Lawrence Berkeley National Laboratory
LBL Publications

Title
Synthetic Control of Water-Stable Hybrid Perovskitoid Semiconductors

Permalink
https://escholarship.org/uc/item/5dh00609

Authors
Kim, Jiyoon
Ghosh, Soumyadeep
Smith, Nicholas WG
et al.

Publication Date
2024-10-23

DOI
10.1002/adma.202406274

Copyright Information

Peer reviewed

Synthetic Control of Water-Stable Hybrid Perovskitoid Semiconductors

Jiyoon Kim, Soumyadeep Ghosh, Nicholas W. G. Smith, Sunhao Liu, Yixuan Dou, Carla Slebodnick, Giti A. Khodaparast, Jin Qian, and Lina Quan*

Hybrid metal-halide perovskites and their derived materials have emerged as the next-generation semiconductors with a wide range of applications, including photovoltaics, light-emitting devices, and other optoelectronics. Over the past decade, numerous single-crystalline perovskite derivatives have been synthesized and developed. However, the synthetic methods for these derivatives mainly rely on acidic crystallization conditions. This approach leads to crystals comprising metal halide building blocks, which show problematic stability when directly exposed to water. In this study, a methodology is developed for synthesizing hybrid metal-halide compounds using lead iodide and the zwitterionic bifunctional molecule cysteamine (CYS), to form various perovskitoid structures under a broad pH range. Interestingly, the different pH conditions alter the coordination environment of lead halides, leading to lead-sulfide and lead-nitride covalent bond formation. This modification significantly enhances their stability when in direct contact with water, lasting for months. Photoluminescence measurements and first principal density functional theory (DFT) calculations reveal that the perovskitoids synthesized under basic and acidic pH conditions exhibit a direct bandgap nature, while those synthesized under neutral conditions display an indirect bandgap. This approach opens new avenues for manipulating synthetic methods to develop water-stable hybrid semiconductors suitable for a wide range of applications, such as solid-state light emitters.

1. Introduction

The synthetic methods for synthesizing polycrystalline thin films[1–4] and single crystals[5,6] of organic-inorganic lead halide perovskites have been developed extensively over the past decade. The synthesis of single crystals typically involves near room-temperature self-assembly of cations and anions into their thermodynamically favored crystal phase.[7] Acidic conditions are often used to protonate organic amines into ammonium cations.[8,9] This process induces the self-assembly of metal halides that coordinate with ammonium cations through ionic-bonding interactions and usually generate crystals that cannot withstand direct contact with water. Under non-acidic conditions, bifunctional organic compounds that can form zwitterions, such as alkylammonium sulfides, can function as both cationic A site and anionic X site in hybrid perovskites of formula ABX (A = organic cation, B = metal, X = Lewis base coordinated to the metal, traditionally a halogen anion).[10] Organic diprotic compounds can dissociate into protonated cations or anionic forms under different pH conditions. Thus, we aim to use bifunctional diprotic organic compounds as our organic motif and adjust pH to diversify the coordination environment of lead, introducing covalency between the organic group and the lead halide.

A recent study used zwitterionic organic compounds in the synthesis of copper and lead hybrid perovskites.[11] The copper chloride hybrid perovskites involved bifunctional alkylammonium acids, RCOOH (4-(ammoniomethyl)

J. Kim, S. Liu, Y. Dou, C. Slebodnick, L. Quan
Department of Chemistry
Virginia Tech
Blacksburg, VA 24061, USA
E-mail: linaquan@vt.edu

S. Ghosh, J. Qian
Chemical Sciences Division
Lawrence Berkeley National Laboratory
Berkeley, CA 94720, USA
N. W. G. Smith, G. A. Khodaparast
Department of Physics
Virginia Tech
Blacksburg, VA 24061, USA
L. Quan
Department of Materials Science and Engineering
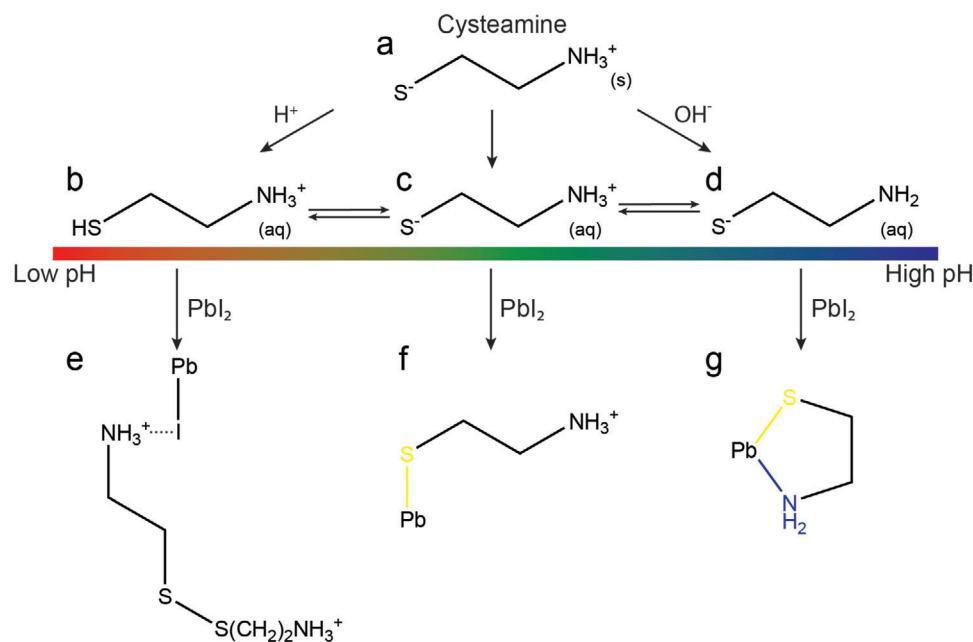Virginia Tech
Blacksburg, VA 24061, USA

Figure 1. Proposed reaction mechanisms of the protonation process of cysteamine under various pH conditions. a) cysteamine in solid form, b) the form of cysteamine under acidic conditions, c) the zwitterionic form of cysteamine under neutral (slightly basic) conditions, d) the form of cysteamine under basic conditions, e) the hydrogen bonding between Pb and I in acidic condition, f) the coordination Pb-S in neutral condition, and g) the coordination of Pb-S and Pb-N in basic condition.

benzoic acid) and RPO$_3$H (3-(ammoniopropyl)phosphonic acid), to synthesize (RCOOH)$_2$CuCl$_4$ and (RPO(OH)$_2$)$_2$CuCl$_4$.[11] In these structures, the Cu forms Jahn-Teller distorted octahedral geometry with the elongated axis parallel to the perovskite slab, similar to other Cu(II)-Cl perovskites. Perovskite (H$_3$O)$_2$(taurine)$_2$CuCl$_4$ features a neutral zwitterionic taurine (NH$_3$(CH$_2$)$_2$SO$_3$H) with H$_3$O$^+$ in the organic layer to neutralize the total crystal charge. A lead-based heterostructure using the acidic form of cysteamine (NH$_3$(CH$_2$)$_2$S) was employed to produce, (Pb$_2$Cl$_2$)(CYS)$_2$PbCl$_4$, through intergrowth methods.[11] Building on the previous approach in synthesizing zwitterion-based perovskites, we proceed to explore the role of pH on the structure of CYS-lead-iodide hybrid perovskites, with the goal of making inroads with the challenge of water stability.

Here, we present a novel synthetic strategy for lead halide perovskites using the bifunctional alkyl ammonium sulfide, cysteamine. By varying pH during synthesis, we obtained three different crystal structures of cysteamine lead halide perovskite derivatives, named perovskitoids. Under acidic conditions, a previously reported compound is formed,[12] with a "traditional" hybrid layered perovskites structure with only non-bonding interactions between the organic cation and the inorganic layer. Under neutral and basic synthetic conditions, first, the sulfur (neutral form) and then both the sulfur and the nitrogen (basic form) have lone pairs that coordinate directly to the lead, while still maintaining layered structures. With the formation of covalent bonds between the organic and inorganic components, the material's water stability increased from a time scale of minutes to months. While previous work has explored the use of cysteamine as a zwitterion in various applications such as radioprotection, treatment of cystinosis, cancer therapy, and as a depigmenting

agent in dermatology,[13] our study is to systematically investigate the effect of pH on cysteamine-lead-iodide crystal structures. Through this approach, we show how pH manipulation can be utilized to rationally design perovskite or perovskitoid structures with increased stability, which is a novel strategy in the field of stable semiconductors for various optical and electronic applications. Utilizing first-principle density functional theory (DFT) calculations, we determined that the perovskitoids synthesized under basic and acidic conditions exhibit a direct bandgap nature, while the perovskitoid synthesized under neutral conditions displays an indirect bandgap nature. Photoluminescence (PL) measurements were carried out on the three perovskitoids, revealing strong excitonic properties that are temperature-dependent. The time-resolved PL measurements indicate that distortions in the inorganic layer impact carrier recombination kinetics. Our novel approach to synthesizing perovskitoids with cysteamine resulted in perovskitoids that displayed unique properties and improved water stability. The instability of hybrid perovskites in humid conditions presents a significant barrier to their practical applications such as solid-state light emitters. Our novel method for creating water-stable hybrid semiconductors provides opportunities to modify synthetic techniques, enabling the efficient use of hybrid perovskites across a wide range of applications.

2. Results and Discussion

2.1. Synthesis

The synthesis of three hybrid perovskite derivatives – perovskitoids, involved the use of cysteamine in three different

protonation states. Cysteamine possesses terminal amine and thiol groups, each of which adopts different protonation states as a function of pH ($^+NH_3(CH_2)_2SH$ at pH < 8.19, $^+NH_3(CH_2)_2S^-$ at 8.19 < pH < 10.75, and $NH_2(CH_2)_2S^-$ at pH > 10.75).[13] In solid form, cysteamine exists as a zwitterion with a protonated amine and deprotonated sulfur to give a neutral species ($^+NH_3(CH_2)_2S^-$, CYS$^{+/-}$, **Figure 1a**). In an acidic solution, both the amine group and thiol group are protonated, to give cationic ammonium, a neutral thiol, and an overall charge of positive one on the species ($^+NH_3(CH_2)_2SH$, CYS$^{+/0}$, Figure 1b). The Fourier transform infrared (FT-IR) spectroscopy reveals an N-H stretching peak from $-NH_3^+$ at 2995 cm^{-1}[14] and an S—H stretching peak at 2571 cm^{-1}[15] in an aqueous solution at pH −1.3, as shown in Figure S1 (Supporting Information). From ^{1}H nuclear magnetic resonance (NMR) analysis, alkane peaks at 2.57 and 2.94 ppm[16,17] thiol peak at 1.95 ppm,[18] and a small peak of ammonium at 7.50 ppm[19] are observed from CYS in D$_2$O with HCl at pH −0.1(Figure S2c,f, Supporting Information). At neutral (slightly basic pH value), the nitrogen remains protonated as the ammonium cation, but the thiol group is deprotonated to give a thiolate anion. Thus, the species is neutral/slightly basic, but each terminal is charged to give a zwitterion ($^+NH_3(CH_2)_2S^-$, CYS$^{+/-}$, Figure 1c). An N—H stretching peak from $-NH_3^+$ at 2920 cm^{-1}[14] is detected at pH 9.0 during FT-IR analysis (Figure S1, Supporting Information). From ^{1}H NMR, alkane peaks at 2.57 and 2.69 ppm[16,17] are detected from CYS in D$_2$O with NaOD at pH 9.0 (Figure S2b,e, Supporting Information). Due to the NMR solution being prepared with NaOD in a D$_2$O solution that lacks hydrogen, the ammonium peak is absent. In the basic solution, further deprotonation takes place at the ammonium group, to give a neutral amine at one terminal, a thiolate anion at the other terminal, and a species with a net charge of negative one ($NH_2(CH_2)_2S^-$, CYS$^{0/-}$, Figure 1d). The FT-IR analysis shows that the N—H stretching peak at 3300 cm^{-1}[14] from $-NH_2$ is present at pH 13.3 (Figure S1, Supporting Information). The alkane peaks at 2.33 and 2.46 ppm,[16,17] along with the amine peak at 1.00 ppm, confirm the structure of CYS in D$_2$O with NaOD at pH 13.3 (Figures S2a,d, Supporting Information). Consequently, we sought that altering the protonation state of cysteamine would impact the coordination environment of the lead halide.

The synthetic procedure of the perovskitoids involved mixing CYS, PbI$_2$, and NaI, and using HI or NaOH solution to control the pH. The slow-cooling crystallization method involved dissolving the desired precursors in water at 110 °C and then slowly cooling down to facilitate single-crystal formation. The three perovskitoids formed have the formulas ($^{+/0}$CYS-CYS$^{+/0}$) PbI$_4$ (acidic, pH -1.3), (CYS$^{+/-}$)PbI$_2$ (neutral, pH 7.7), and (CYS$^{0/-}$)PbI (basic, pH 13.2). In the acidic form, the cysteamine dimerized to form a disulfide bond, with the ammonium groups at both termini of the dimer engaging in N—H⋯I hydrogen bonding with the inorganic layers (Figure 1e). (In this work, we are defining a hydrogen bond as an N—H⋯X interactions where X = I or S, and the H⋯X distance is the sum of the vdW radii − 0.2 Å.) In the neutral perovskitoid, when the pH of the solution is 7.7, 24.5% of cysteamine exists as CYS$^{+/-}$(zwitterion), and 75.5% of cysteamine has the form of CYS$^{+/0}$ in equilibrium based on Henderson-Hasselbalch equation ($pH = pK_a + \log_{10}\frac{[A^-]}{[HA]}$) with the pKa = 8.19 of thiol in CYS. A lone pair of

electrons on the neutral S-terminal is available to form a covalent bond with lead while the ammonium group is available to form N—H⋯S and N—H⋯I hydrogen bonds (Figure 1f). The lead sulfide bonds should elevate the formation energy of hybrid perovskites and enhance stability. In the basic perovskitoid, the neutral amine is capable of hydrogen bonding, but also has a lone pair of electrons to form a covalent bond with lead (Figure 1g). The Pb—N bonding is expected to further enhance water stability.

2.2. Single-Crystal X-Ray Diffraction and Raman Spectra

All three compounds form alternating inorganic/organic layers that comprise distorted octahedral lead halides. The crystallographic data and structure refinement information are summarized in Tables S1–S4 (Supporting Information).

2.2.1. ($^{+/0}$CYS-CYS$^{+/0}$)PbI$_4$ (Acidic)

Orange plates that crystallized in the monoclinic space group $P2_1/n$ with formula $C_4H_{14}I_4N_2PbS_2$ (($^{+/0}$CYS-CYS$^{+/0}$)PbI$_4$), which is equivalent to a Ruddlesden-Popper (RP) phase 2D perovskite $A_2B_nX_4$ ($n = 1$) as shown in **Figure 2a**. The crystals were synthesized from a solution of NaI (aq) with a small amount of HI (aq) in addition to the precursors CYS and PbI$_2$. The inorganic component comprises single layers of corner-sharing distorted PbI$_6$ octahedral running parallel to the (001) plane (Figure 2d; Figure S3a, Supporting Information). The organic $^{+/0}$CYS-CYS$^{+/0}$ cations sit between layers and are oriented with the terminal ammonium groups directed toward the terminal iodide atoms, such that all three hydrogen atoms of each amine form N—H⋯I hydrogen bonds. These hydrogen bonds play a role in maintaining the 2D structure of the crystal. The formation of hydrogen bonds between the amine groups and sulfur atoms is hindered by the presence of organic cations that have disulfide bonding in these acidic crystals. The structure is dependent on the hydrogen bonding interactions between the ammonium groups and the iodine atoms in the inorganic layers. As is typical of most layered hybrid perovskites, no covalent bonding interactions exist between the organic and inorganic components in the structure. Figure 2g and Table S5 (Supporting Information) show the Raman spectrum of the acidic form. The peaks at 25.2, 30.9, 46.1, 65, 83.8, and 112.1 cm^{-1} are attributed to Pb—I vibrations in the octahedra.[20] The bump at ≈200 cm^{-1} in Figure 2g is a torsional vibration of CYS at room temperature.[21,22] The consistency in Pb—I vibrations across the three crystals (acidic, neutral, and basic) suggests a shared structural element, while specific Raman peaks offer unique bonding arrangements in each crystal (Table S5, Supporting Information). We then use X-ray photoemission (XPS) spectroscopy to analyze the surface atomic environment. As the crystal contains thiol and ammonium, we could determine the binding states of sulfur and nitrogen. The observed 163.6 eV peak for S 2p indicates that the form of sulfur is —SH.[23] The 401.0 eV peak for N1s corresponds to the —NH$_3^+$ (Figure S3, Supporting Information).[24]
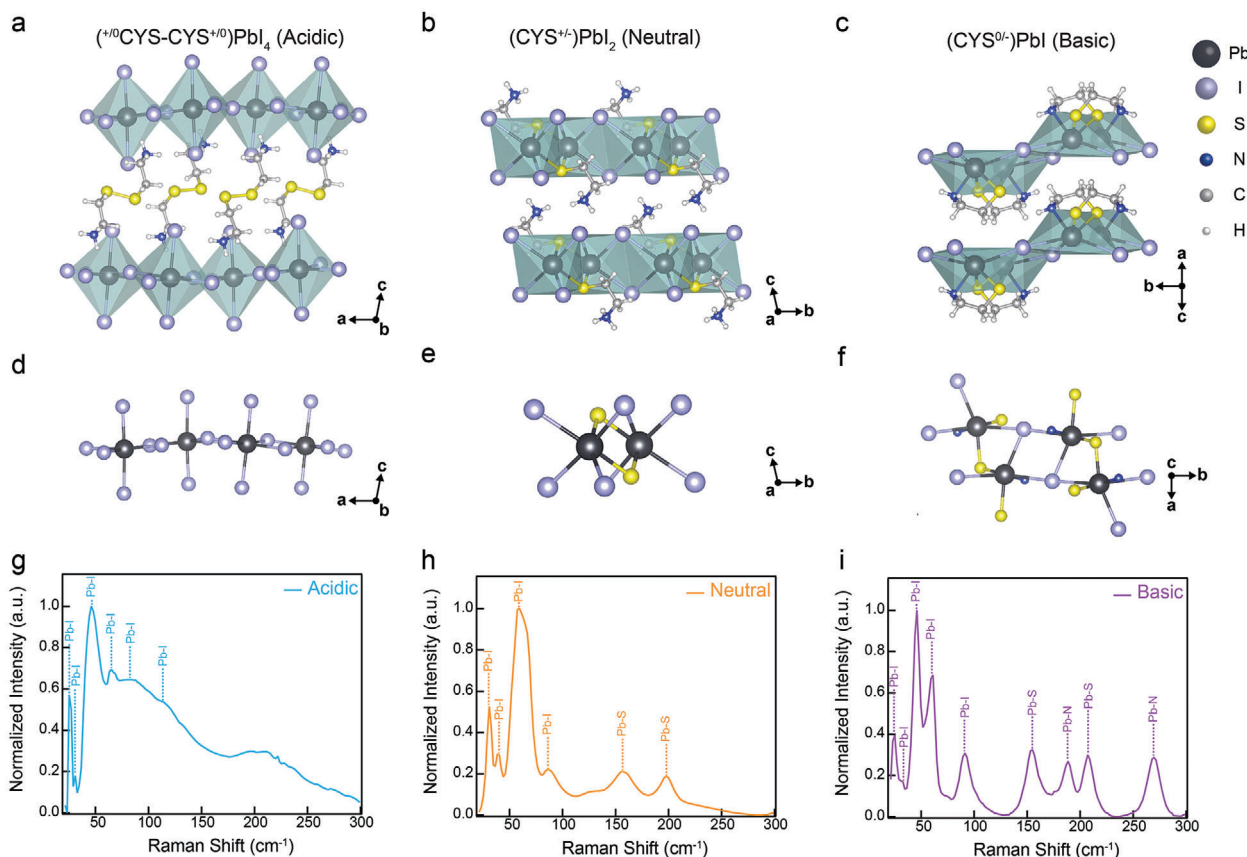
Figure 2. Crystal structures that synthesized at different pH conditions. a) crystal structure of $(^{+/0}CYS-CYS^{+/0})PbI_4$ in acidic condition (pH −1.3). b) crystal structure of $(CYS^{+/−})PbI_2$ in neutral condition (pH 7.7). c) Crystal structure of $(CYS^{0/−})PbI$ in basic condition (pH 13.2). d) corner-sharing octahedra connectivity in acidic condition. e) edge-sharing octahedra connectivity in neutral conditions f) edge-sharing octahedra connectivity in basic conditions. Raman spectra of g) $(^{+/0}CYS-CYS^{+/0})PbI_4$ in acidic condition (pH −1.3), h) $(CYS^{+/−})PbI_2$ in neutral condition (pH 7.7) and i) $(CYS^{0/−})PbI$ in basic condition (pH 13.2).

2.2.2. $(CYS^{+/−})PbI_2$ (Neutral)

Yellow plates that crystallized in the triclinic space group P $\bar{1}$ were obtained from a solution of PbI_2 (3.412–3.580 Å) and CYS·HCl in NaI (aq) as shown in Figure 2b. The inorganic layer comprises highly distorted PbI_4S_2 octahedra with four long Pb—I bonds and two shorter Pb—S bonds. Each octahedron is edge-sharing with three neighboring octahedra to form distorted honeycomb sheets that run parallel to the (001) plane (Figure 2e; Figure S4b, Supporting Information). The Pb—S bonds are on opposite faces of the inorganic layers and direct the ammonium group away from the inorganic layer. A detailed analysis of the hydrogen bonding interactions reveals a complex network. The structure exhibits four distinct N—H•••A hydrogen bonds, where A (acceptor) represents either iodine or sulfur atoms. Specifically, the N1—H1a•••I1 interaction has a H•••A distance of 2.767 Å and a D (donor)•••A distance of 3.552(3) Å. The N1—H1b•••S1 bond shows a H•••A distance of 2.702 Å and a D•••A distance of 3.376(3) Å. There are two additional interactions: N1—H1c•••I1 with a H•••A distance of 3.047 Å and a D•••A distance of 3.650(3) Å, and N1—H1c•••I2 with a H•••A distance of 3.026 Å and a D•••A distance of 3.682(3) Å. These hydrogen bonding interactions play a crucial role in the crystal packing, with two of the

ammonium hydrogens interacting with neighboring PbI_4S_2 layers by forming one N—H•••I hydrogen bond and one N—H•••S hydrogen bond. In the Raman spectrum of the neutral form in Figure 2h, peaks at 157.0 and 197.9 cm^{-1} were assigned to Pb—S vibrations[25] and peaks below 100 cm^{-1} (30.9, 40.4, 59.3, and 87.6 cm^{-1}) were assigned to Pb—I vibrations (Table S5, Supporting Information).[20] The 161.5 eV peak for S2p in XPS measurement confirms that the binding state of sulfur is present as —S^{-}.[23] The 399.8 eV binding energy for N1s is not exactly in the range of —NH$_3^+$ (401–402eV)[26] (Figure S3, Supporting Information). The peak shift would be caused by the electronic environment of a nitrogen atom in the crystal surrounded by iodide that can have hydrogen bonding between iodide and hydrogen which can enhance the electron density of nitrogen to give a slightly lower binding energy for ammonium.[27]

2.2.3. $(CYS^{0/−})PbI$ (Basic)

Colorless plates that crystallized in the monoclinic space group $P2_1/n$ were obtained from a solution of PbI_2 and CYS in NaI (aq) with NaOH (aq) added to adjust pH. The inorganic layer comprises highly distorted PbI_3S_2N octahedra with three long

**ADVANCED
SCIENCE NEWS**

www.advancedsciencenews.com

**ADVANCED
MATERIALS**

www.advmat.de

Pb—I bonds (3.412–3.580 Å) and three shorter Pb—S and Pb—N bonds (2.440–2.856 Å). Each octahedron is edge sharing through the I and S atoms with three neighboring octahedra to form zigzag layers that run parallel to the (10$\bar{1}$) plane (Figure 2c,f; Figure S4c, Supporting Information). The CYS$^{0/-}$ are bidentate and cover the surface to form a hydrophobic organic layer between the inorganic layers. To analyze hydrogen bonding interaction, we found two distinct N—H•••A hydrogen bonds, where A represents either iodine or sulfur atoms. The N1—H1a•••I1 interaction has a H•••A distance of 2.943 Å, and a D•••A distance of 3.760(5) Å. The N1—H1b•••S1 bond shows a H•••A distance of 2.991 Å and a D•••A distance of 3.671(4) Å. These hydrogen bonds help maintain the crystal structure together by linking the inorganic layers with the organic molecules. The Raman spectrum in Figure 2i reveals distinctive vibrational features. Raman shifts below 100 cm^{-1} (25.2, 32.8, 46.1, 61.2, and 91.4 cm^{-1}) are attributed to Pb—I vibrations[20] and peaks at 155.1 and 207.2 cm^{-1} correspond to Pb—S vibrations.[28,29] Additionally, peaks at 188.6 and 269.9 cm^{-1} correspond to Pb—N vibrations and consistent with the Pb—N covalent bonding vibrational mode (Table S5, Supporting Information).[30,31] The 161.5 eV XPS peaks for S2p from the basic crystal support that the binding state of sulfur is in the —S$^-$ form.[23] The 398.9 eV peak is found, corresponding to —NH$_2$ (Figure S3, Supporting Information).[32] It can be inferred that an amine group is present in the crystal and is bound to lead.

When comparing the three perovskitoids, the structure of the acidic form most closely resembles a "traditional" hybrid perovskite, featuring distinct metal halide and organic layers. Under neutral pH, the inorganic/organic layer structure is maintained, but the sulfide covalently bonds to lead (Pb), directly linking the inorganic and organic layers. Under basic conditions, both the nitrogen (N) and sulfur (S) atoms from CYS covalently bond to lead (Pb), forming single inorganic/organic layers where the inorganic component is located inside and surrounded by a hydrophobic organic surface. In addition, N—H⋯X (X = I, S) hydrogen bonds form in all three structures, but the number of hydrogen bonds per N-atom decreases from three to two to one for the acidic, neutral, and basic perovskitoids, respectively. Therefore, as the pH increases, the increased covalency between the organic and inorganic layers should result in more stable structures. The Pb—S and Pb—N covalent bonding both increases the strength of the interactions between the organic and inorganic components in the structure and makes it more difficult for water to penetrate and interact with these hydrophilic functional groups to trigger decomposition.

2.2.4. Stability of Perovskitoids

The stability of the three perovskitoids upon direct contact with water was monitored over time using powder-XRD (PXRD) and optical microscopy (Figures S5 and S6, Supporting Information). As illustrated in **Figure 3a**, the PXRD pattern of the basic form remained unchanged, maintaining the structure of the fresh sample even after one month of storage in water. This observation suggests that the covalency between lead sulfide and lead nitride plays a crucial role in enhancing the stability of the crystals. Crystals synthesized under neutral conditions also exhibited

no distinct changes in the PXRD pattern after one month in water (Figure 3b). Then we assessed their stability in a strong basic solution of 0.1 $_M$ KOH, as illustrated in Figure 3c. Interestingly, crystals synthesized under basic conditions retained their original structure for up to 7 days, whereas those synthesized under neutral conditions remained stable for only 6 h. Beyond this timeframe, the crystal structure transformed from (CYS)PbI$_2$ to (CYS)PbI (i.e., the structure of crystals synthesized under basic conditions). Finally, we examined the water stability of the acid form (Figure 3d). The crystals decomposed into starting material (PbI$_2$) within 1 day, with the CYS presumably remaining in solution. The black dots in the top pattern in Figure 3d are aligned with the PXRD pattern of PbI$_2$. As expected, the lack of covalent bonds between the inorganic PbI$_2$ framework and the organic CYS, resulted in immediate degradation upon direct contact with water.

The exceptionally high stability of the basic and neutral forms compared to the acidic form suggests that the covalent bonds between the organic and inorganic components in the layer structures are critical to the materials' stability. We believe that in the acidic form, the water interferes irreversibly with the hydrogen bonding network, triggering the decomposition of the compounds back into their starting materials. Formation of covalent bonds between the organic and inorganic components, while still maintaining the general hybrid perovskite structure features, may provide a means to generate more stable materials while maintaining important properties. Besides the water stability, all three crystals showed quite decent thermal stability at above 200 °C (Figure S7, Supporting Information). The thermal stability is attributed to the interaction between multi-functional CYS and inorganic structure.

2.2.5. Optical Properties

To investigate the optical properties of the three perovskitoids, we conducted diffuse reflectance spectroscopy to analyze their optical absorption and corresponding bandgap. The absorption spectra were observed in the range between 420 nm to 550 nm for all three crystals. Bandgap energies were determined through Tauc plots, plotting $(F(R)h\nu)^2$ against photon energy and converting photon energy to wavelength (**Figure 4a,b**). The calculated bandgap energies for the basic, neutral, and acidic crystals were 2.96 eV (419 nm), 2.48 eV (500 nm), and 2.25 eV (551 nm), respectively. Steady-state PL spectra of the three crystals were recorded using a 375 nm continuous wave (CW) laser at room temperature (Figure 4c). The basic crystal displayed PL emissions at both 503 and 578 nm, accompanied by a narrow excitonic emission and a broad trap-state emission, at room temperature. The broad emission is associated with the self-trapped emission (STE).[33] The neutral crystal exhibited excitonic light emission at 512 nm. The acidic crystal showed strong excitonic emission both at 512 and 540 nm, at room temperature. Inset photographs in Figure 4d,e, and f exhibit the basic, neutral, and acidic crystals, respectively, under UV illumination (365 nm). These images provide a visual representation of the distinct emission characteristics for each crystal type. The basic crystal exhibited a white light emission, while the neutral crystal displayed a yellowish-green
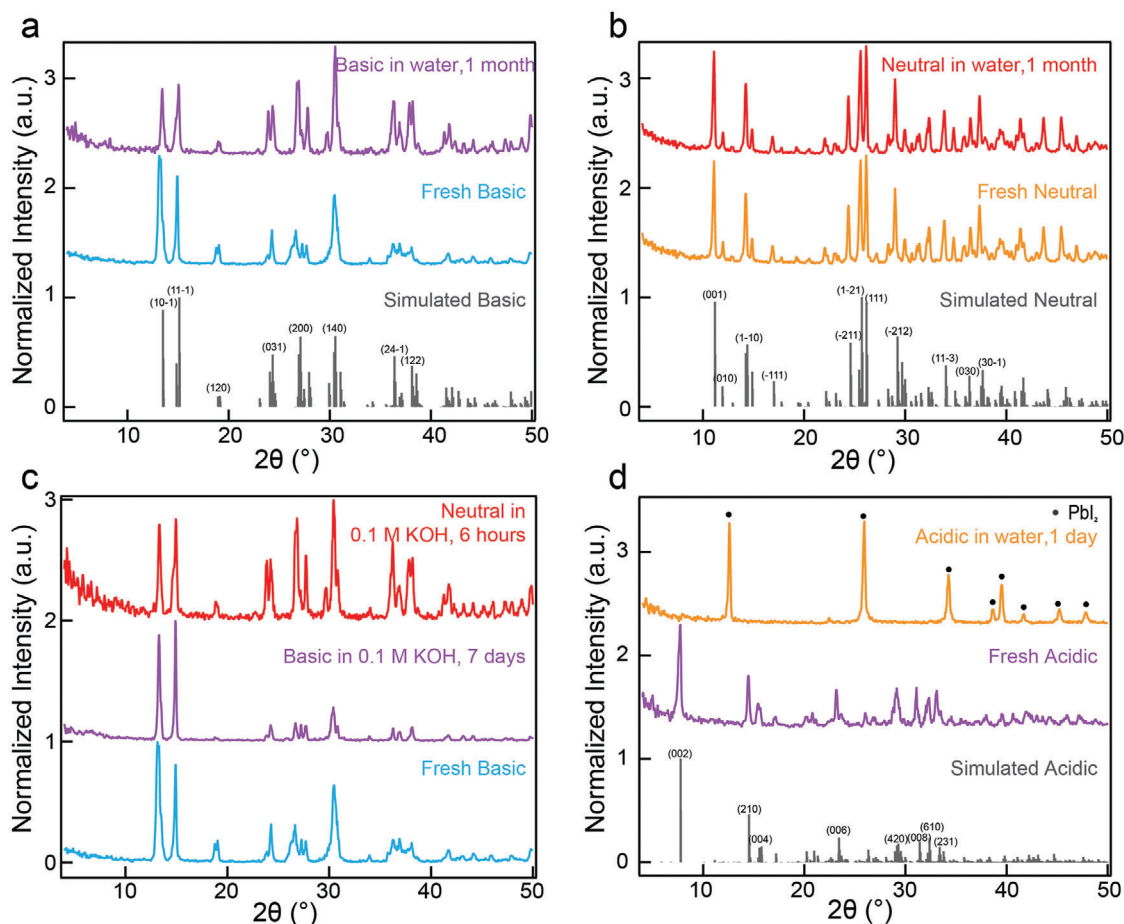
2406274 (5 of 11)

ADVANCED
SCIENCE NEWS

www.advancedsciencenews.com

ADVANCED
MATERIALS

www.advmat.de

Figure 3. The structural stability of CYS perovskitoids. a) PXRD patterns of basic crystal and the stability check in water. b) PXRD patterns of neutral crystal and the stability check in water. c) PXRD stability test of basic and neutral crystals under a strong base (0.1M KOH (aq)) solution. d) PXRD patterns of acidic crystal after exposure to the water.

emission. The acidic crystal appeared green under UV light. These visual observations align with the measured PL emission peaks and offer a demonstration of the potential optical display applications.

We then measured time-resolved PL (TRPL) to determine the carrier/exciton recombination kinetics. TRPL experiments were conducted on single crystals employing a pulsed fs-laser with a repetition rate of 80 MHz and wavelength of 400 nm with a fluence of 0.17 µJ cm^{-2}. The observed PL decay time and emission wavelengths varied across the crystals. For the basic crystal, the PL decay time was 1.10 ± 0.18 ns with emission at 470 nm (Figure 4d; Table S6, Supporting Information). The neutral crystal showed a shorter decay time of 0.80 ± 0.12 ns with emission at 516 nm (Figure 4e; Table S6, Supporting Information). The acidic crystal displayed the shortest decay time at 0.29 ± 0.0077 ns with emission at 540 nm (Figure 4f; Table S6, Supporting Information). These results suggest that the longer decay time for the basic crystal implies slower recombination of charge carriers compared to the neutral and acidic crystals.[34] To investigate the relationship between the PL decay time and structure of crystals, the octahedral distortion (Δd) was calculated based on Pb-X bond lengths and the bond angle

variance (σ^2) was calculated based on the X-Pb-X angle in the octahedra.

$$\Delta d = \left(\frac{1}{6}\right) \sum_{n=1}^{6} \left[\frac{d_n - d_{avg}}{d_{avg}}\right]^2 \tag{1}$$

where d_{avg} is the average Pb—X bond distance and d_n are the six Pb—X bond distances (X = I, N, and S).

$$\sigma^2 = \left(\frac{1}{11}\right) \sum_{n=1}^{12} \left(\theta_n - 90\right)^2 \tag{2}$$

where θ_n is each X-Pb-X angle (X = I, N, and S).

The average PL decay time was calculated to reveal the trap-state emission between the three crystals.

$$\tau_{avg} = \frac{\sum_i A_i \tau_i}{\sum_i A_i} \tag{3}$$

where τ_{avg} is an average PL decay time, A_i are amplitude of ith PL decay time, and τ_i are i^{th} PL decay time.

**ADVANCED
SCIENCE NEWS**

www.advancedsciencenews.com
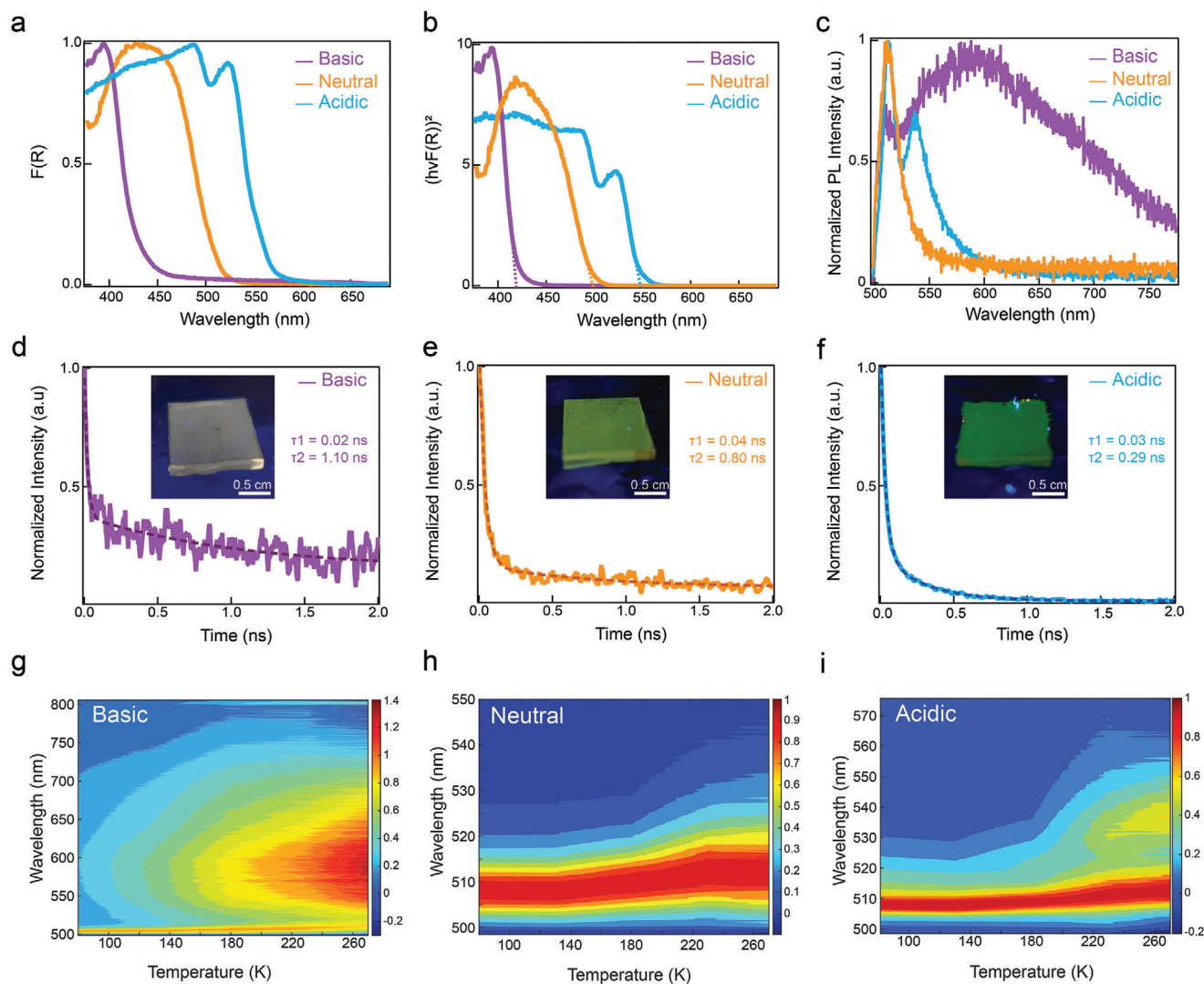
**ADVANCED
MATERIALS**

www.advmat.de

Figure 4. Optical properties of CYS perovskitoid single crystals. a) Diffuse reflectance spectra of three perovskitoids. b) Tauc plots of perovskitoids. c) PL spectra of perovskitoids at room temperature. Time-resolved PL of d) basic e) neutral f) acidic crystals, with inset photographs showing the respective luminescent crystals under UV illumination. 2D temperature-dependent PL spectra of g) basic h) neutral i) acidic crystals.

Basic, neutral, and acidic crystals had significantly different values in the octahedral distortion (Δd) of 196.56×10^{-4}, 67.42×10^{-4}, and 2.16×10^{-4}, respectively (**Table 1**; Table S7, Supporting Information). In addition to Δd, the bond angle variance (σ^2) in octahedral of basic, neutral, and acidic crystals were 340, 98, and 10, respectively (**Table 1**; Table S7, Supporting Information). We discovered that the distortions in the octahedra of the basic crystal were caused by the Pb—N and Pb—S bonding in the PbI$_2$ framework, leading to the most distorted inorganic structure among the three crystals. The basic crystal with highly distorted octahedra showed both band edge exciton emission and STEs and had the longest τ_{avg} of 0.28 ns (**Table 1**; Table S8, Supporting Information) out of the three crystals.[35,36] The neutral crystal had τ_{avg} of 0.10 ns which was longer than the acidic crystal's τ_{avg} of 0.08 ns

Table 1. The octahedral distortion (Δd), the bond angle variance (σ^2), and average PL decay time (τ_{avg}) of (CYS$^{0/-}$)PbI (basic), (CYS$^{+/-}$)PbI$_2$ (neutral), and ($^{+/0}$CYS-CYS$^{+/0}$)PbI$_4$ (acidic) crystals.

	(CYS$^{0/-}$)PbI (Basic)	(CYS$^{+/-}$)PbI$_2$ (Neutral)	($^{+/0}$CYS-CYS$^{+/0}$)PbI$_4$ =(Acidic)
Δd	196.56×10^{-4}	67.42×10^{-4}	2.16×10^{-4}
σ^2	340	98	10
τ_{avg} (ns)	1.10 ± 0.18	0.80 ± 0.12	0.29 ± 0.0077

**ADVANCED
SCIENCE NEWS**

www.advancedsciencenews.com
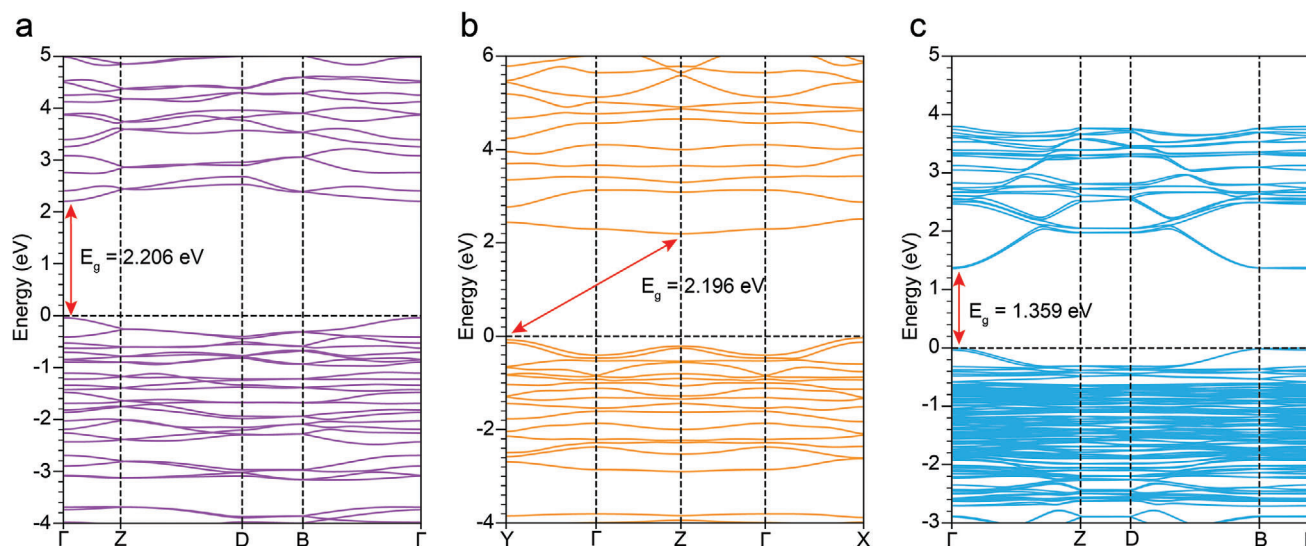
**ADVANCED
MATERIALS**

www.advmat.de

Figure 5. Electronic band structures from a) basic crystal, b) neutral crystal, and c) acidic crystal with corresponding bandgap energy.

(Table 1; Table S8, Supporting Information). Because of the Pb─S bonding, the neutral crystal was much more distorted than the acidic crystal, leading to a longer PL decay time than the acidic crystal.

To further explore the photophysical properties at elevated temperatures, temperature-dependent PL measurements were conducted. As the sample was cooled from 270 to 80 K, the PL intensity of the basic crystal was enhanced with decreasing temperature, while the STE intensity diminished (Figure 4g). The full width at half maximum (FWHM) of the PL spectrum from the neutral crystals became narrower as temperature decreased with a slight blue shift of ≈4 nm (Figure 4h). This suggests that non-radiative recombination mechanisms were suppressed at lower temperatures. In Figure 4i, the acidic crystal had PL maximum at 512 and 540 nm at 270 K. However, as the temperature decreased, the PL intensity at 540 nm nearly disappeared. This indicates that the emission at the band edge became dominant as trap-state emission diminished at lower temperatures.

2.2.6. DFT Electronic Structure Calculations

We utilized the generalized gradient approximation of density functional theory (GGA-PBE) to compute the electronic band structures of three compounds. Incorporating the spin-orbit coupling (SOC) effect, the calculated bandgaps for the basic, neutral, and acidic crystals are 2.206 eV (**Figure 5a**), 2.196 eV (Figure 5b), and 1.359 eV (Figure 5c), respectively. This trend indicates that the bandgap becomes smaller as the pH level decreases, consistent with the observations from optical diffuse reflectance measurements. Specifically, the neutral compound exhibits an indirect band gap, while both the basic and acidic compounds display direct band gaps. Notably, the basic compound, characterized by edge-sharing connectivity, displays a relatively flat energy dispersion for both the valence band (VB) and conduction band (CB). In contrast, the neutral crystal, with edge-sharing connectivity, exhibits a more dispersed energy band at the conduction band. The

band structure of the acidic crystal with corner-sharing connectivity, demonstrates greater dispersion, aligning with the typical characteristics observed in 2D hybrid perovskites.

2.2.7. Application to the Water Stable Thin Film Display

To demonstrate the potential display applications, we have fabricated single crystal/polystyrene (PS) composite thin films and studied water stability. To create solution-processable semiconductor ink that could be used for thin films, ground neutral crystals were uniformly dispersed in a PS matrix. A simple display was created that functioned both in air and water to demonstrate the material's capabilities. The thin film with the VT logo (which stands for Virginia Tech) appeared as a yellow pattern under normal lighting conditions (**Figure 6a**). This demonstrated the successful integration of the neutral crystal/PS composite to form a distinct logo on the film surface. After excitation with UV light (365 nm), the thin film showed a clear emission of a green VT logo in the air (Figure 6b). It was remarkable that despite being fully submerged in water, the film retained its luminescent properties and displayed the VT logo with comparable brightness and clarity (Figure 6c). This demonstration in both air and water highlights the exceptional stability of the neutral crystal/PS composite. The material retains its structure and luminescent properties in dry conditions and when submerged in water. These demonstrations show the potential of neutral crystal/PS composite thin films for water-resistant light-emitting displays. They could be useful in wet environments where normal moisture-sensitive materials (halide perovskites) would quickly decompose.

3. Conclusion

Our study presents a systematic approach to synthesizing hybrid metal-halide perovskites and perovskitoids, introducing an innovative approach to enhance water stability and optical properties.
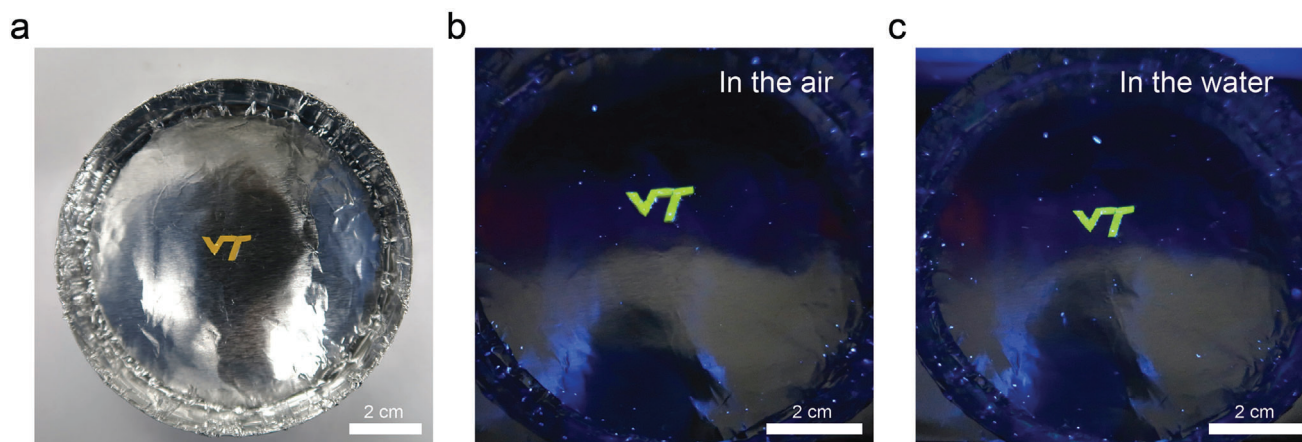
**ADVANCED
SCIENCE NEWS**

www.advancedsciencenews.com

**ADVANCED
MATERIALS**

www.advmat.de

Figure 6. a) Thin film of neutral crystal/PS composite. Emission of neutral crystal/PS composite thin film under UV light (365 nm) b) in the air, and c) in the water.

The use of cysteamine, a bifunctional organosulfide, enabled us to change the coordination environment of lead halides under different pH conditions. The perovskitoids (CYS)PbI, (CYS)PbI$_2$, and (CYS-CYS)PbI$_4$ that were produced under basic, neutral, and acidic conditions had distinct crystal structures and bonding configurations. Our strategy resulted in the formation of lead-sulfide and lead-nitride covalent bonds in the crystal structures under basic and neutral conditions, which improved their stability from hours for the acidic form to over a month for the neutral and basic forms. Optical measurements revealed intriguing bandgap variations among the perovskitoids, with a direct bandgap observed in the basic and acidic forms, and an indirect bandgap for the neutral form. By observing excitonic properties through PL measurements, we can further demonstrate the potential of these materials for optoelectronic applications. This work opens new avenues for tailoring the properties of hybrid metal-halide perovskites by manipulating synthetic conditions, providing a foundation for designing water-stable semiconductors with tunable optical properties. These advancements will benefit a variety of applications, including solid-state light emitters and optoelectronic devices.

4. Experimental Section

Materials: PbI$_2$ (99%), cysteamine hydrochloride (≥98%), cysteamine ((≥98%), and hydroiodic acid (57 wt% in H$_2$O, distilled, stabilized, 99.95%) were purchased from Sigma-Aldrich and used as received. Sodium iodide (≥99%) was purchased from TCI and used as received.

Synthesis—Basic CYSPbI: (CYS)PbI was synthesized using the slow-cooling crystallization method. Cysteamine (1 mmol) was dissolved in the basic solution mixed with 6M NaI (aq) (10 mL) and 1M NaOH (aq) (2 mL). Afterward, PbI$_2$ (1 mmol) was added to the precursor solution. The reaction mixture was heated to 110 °C for 1 h until everything dissolved. The solution was cooled gradually to room temperature (RT) with a temperature gradient of 4 °C h^{-1}. The colorless crystals were filtered under a vacuum and washed with DI water and acetone.

Synthesis—Neutral (CYS)PbI$_2$: (CYS)PbI$_2$ was synthesized using the slow-cooling crystallization method. Cysteamine hydrochloride (C$_2$H$_7$NS·HCl) (0.6 mmol) was dissolved in the 6M NaI (aq), and PbI$_2$ (0.6 mmol) was added to the solution. The reaction mixture was heated to 110 °C for 1 h until everything dissolved. The temperature of the solution was gradually reduced to RT with a gradient of 4 °C h^{-1}. Yellow crystals

were filtered under a vacuum and washed with distilled (DI) water and acetone.

Synthesis—Acidic (CYS)$_2$PbI$_4$: (CYS)$_2$PbI$_4$ was synthesized using the slow-cooling crystallization method. Cysteamine (1 mmol) was dissolved in the acidic solution mixed with 6M NaI (aq) (5mL) and 57 wt % HI (aq) (1 mL). Afterward, PbI$_2$ (1mmol) was added to the precursor solution. The precursor solution was heated to 100 °C for 1 h until the precursors dissolved. The temperature of the solution was decreased to RT with a gradient of 4 °C h^{-1}. The orange crystals were filtered under a vacuum and washed with chloroform.

Powder XRD: An X-ray diffractometer (Rigaku Mini Flex 600) with a Cu kα (λ = 0.154 nm) radiation source generated at 40 kV and 15 mA, was used to analyze the crystal structure of all crystals. The scanning range, 2θ, of the instrument was between 4° and 50°, the scanning rate was 10° min^{-1}, and the increment was 0.05° per step.

Single-Crystal XRD: The crystals were centered on the goniometer of a Rigaku Oxford Diffraction Synergy-S diffractometer equipped with a HyPix6000HE detector and operating with MoKα radiation. The data collection routine, unit cell refinement, and data processing were carried out with the program CrysAlisPro.[37] The structures were solved using SHELXT[38] and refined using SHELXL[39] via Olex2.[40] The final refinement model involved anisotropic displacement parameters for non-hydrogen atoms and a riding model for all hydrogen atoms. Software Vesta was used for molecular graphics generation.[41] Software Mercury was used for the shortest D-H•••A distances.[42]

Raman Spectroscopy: The acquisition of Raman spectra was done by excitation of a 532 nm laser, and the collection of Raman signals was done with a CCD camera (Horiba XploRA PLUS). The measurements were conducted in ambient conditions. The Raman spectra were obtained using a 10x objective lens.

FT-IR Analysis: CYS was dissolved in pH −1.3, 9.0, and 13.3 aqueous solution and drop-casted. Fourier transform infrared spectroscopy (FT-IR) was performed on a Thermo Scientific Nicolet iS5 spectrometer with an iD7 ATR accessory. The scan range was 4000 – 400 cm^{-1} with 64 scans and a resolution of 0.8 cm^{-1}.

NMR Analysis: Proton nuclear magnetic resonance (^{1}H NMR) spectra were collected in D$_2$O or NaOD on an Agilent U-4 DD2 400 MHz. Carbon NMR (^{13}C NMR) spectra were collected in D$_2$O or NaOD on a Bruker Avance II 500 MHz.

XPS Analysis: X-ray Photoelectron Spectroscopy (XPS) spectra were collected on a PHI 5000 Versaprobe III spectrometer using an aluminum anode X-ray source with a photon energy of 1486.6 eV. Survey spectra were collected with a 25 W, 15 kV source producing a 100 μm beam with a scan range of 1100–0 eV with a step size of 0.5 eV and pass energy of 280 eV.

PXRD Stability Test: A total of 100 mg of crystals were immersed in 5mL of DI water for a given length of time such as 1 day, 1 week, and 1

**ADVANCED
SCIENCE NEWS**

www.advancedsciencenews.com

**ADVANCED
MATERIALS**

www.advmat.de

month. After the soaking time was finished, the crystals were filtered using a vacuum. The structure change or degradation after exposure to water was revealed by comparing the PXRD patterns of fresh crystals.

Diffuse Reflectance: An Agilent Technologies Cary 5000 UV–vis–NIR spectrometer was used to measure diffuse reflectance for solid-state samples using an internal diffuse reflectance accessory.

Time-Resolved PL and Temperature-Dependent PL: A Horiba iHR-550 spectrometer with an LN-cooled CCD Horiba Symphony II detector was used for PL measurements. The samples were excited with a 488 nm CW Coherent Sapphire laser at 1 mW of laser power. The samples were cooled inside a cryostat from 270 to 80 K with time taken between each temperature measurement to allow for proper thermalization. A 488 nm Long Pass Edge filter was used before the spectrometer to eliminate the laser line mixed with the PL response. Exposure times were varied between 1 and 0.1 s to avoid detector saturation at lower temperatures and the entrance slit size into the spectrometer was kept at 0.1 mm.

A PicoHarp 300 was used for TRPL measurements with a Si sync photodetector acting as a starting reference detector and a single-photon avalanche detector (SPAD) was used for counting PL photons. The sync detector was synced/timed with an 80 MHz (13.5 ns between each pulse) Ti:Sapphire Coherent Chameleon laser set at 800 nm. The laser frequency was then doubled to 400 nm using a thick BBO crystal achieving an excitation power of 14 mW. The SPAD cannot differentiate photon energies so to ensure the speak PL peak of interest was only counting, an Acton 2300i spectrometer was utilized acting as a monochromator along with a 450 nm Long Pass filter to remove any laser light. The entrance and exit slits of the monochromator were kept fully open (≈2 mm). The TRPL accumulation time was 120 s. The observed TRPL traces were fitted with a double exponential fit.

DFT Calculations: The electronic structure calculations were conducted utilizing the Quantum Espresso code,[43] employing Density Functional Theory (DFT) in conjunction with plane wave pseudopotentials. Within this framework, the electronic exchange-correlation interactions were accounted for using the generalized gradient approximation (GGA) with the Perdew-Burke-Ernzerhof (PBE) functional.[44] In the computations, non-spin-polarized single-point energy calculations were performed employing the experimental lattice parameters as initial input values. The plane wave cutoff energy for Kohn-Sham valence states was set at 70 Ry for the neutral and basic samples, while for the acidic sample, after conducting convergence tests, it was adjusted to 100 Ry. To sample the Brillouin zone (BZ) in k-space, a grid size of $2 \times 2 \times 1$ was employed for the neutral and basic samples, and $1 \times 1 \times 1$ for the acidic sample, facilitating self-consistent field (SCF) calculations.[45,46] For the pseudopotential data, the Pslibrary database was drawn upon employing ultrasoft pseudopotentials. Throughout the electronic minimization process, a stringent convergence threshold of 10^{-6} eV was applied. Furthermore, the influence of spin-orbit coupling (SOC) was incorporated into these calculations, where collinear spin polarization was assumed, and full relativistic pseudopotentials were utilized to account for this effect.

Fabrication of Neutral Crystal/PS Inks and Display of Thin-Film: A total of 20 mg of PS was dissolved in 0.2 mL of chloroform at room temperature. 30 mg of ground neutral crystal powders were added into the PS solution to make neutral crystal/PS ink. The solution was sonicated for 15 min and drop-casted onto the VT logged frame. After PS was cured, the film peeled off. Neutral crystal/PS composite thin film was illuminated at a 365 nm UV light.

Accession Codes: CCDC 2345785, 2345786, and 2345787 contain the supplementary crystallographic data for this paper. The data can be obtained free of charge via https://www.ccdc.cam.ac.uk/data_request/cif, or by emailing data_request@ccdc.cam.ac.uk, or by contacting The Cambridge Crystallographic Data Centre, 12 Union Road, Cambridge CB2 1EZ, UK; fax: +44 1223 336033.

Supporting Information

Supporting Information is available from the Wiley Online Library or from the author.

Conflict of Interest

The authors declare no conflict of interest.

Data Availability Statement

The data that support the findings of this study are available from the corresponding author upon reasonable request.

[1] J. A. Steele, E. Solano, H. Jin, V. Prakasam, T. Braeckevelt, H. Yuan, Z. Lin, R. de Kloe, Q. Wang, S. M. J. Rogge, V. Van Speybroeck, D. Chernyshov, J. Hofkens, M. B. J. Roeffaers, *Adv. Mater.* **2021**, *33*, 2007224.

[2] W. Zhang, S. Pathak, N. Sakai, T. Stergiopoulos, P. K. Nayak, N. K. Noel, A. A. Haghighirad, V. M. Burlakov, D. W. Dequilettes, A. Sadhanala, *Nat. Commun.* **2015**, *6*, 10030.

[3] W. Nie, H. Tsai, R. Asadpour, J.-C. Blancon, A. J. Neukirch, G. Gupta, J. J. Crochet, M. Chhowalla, S. Tretiak, M. A. Alam, *Science* **2015**, *347*, 522.

[4] P. Fan, D. Gu, G.-X. Liang, J.-T. Luo, J.-L. Chen, Z.-H. Zheng, D.-P. Zhang, *Sci. Rep.* **2016**, *6*, 29910.

[5] A. Poglitsch, D. Weber, *J. Chem. Phys.* **1987**, *87*, 6373.

[6] a) D. G. Billing, A. Lemmerer, *Acta Crystallographica Section B: Structural Science* **2007**, *63*, 735; b) Y. Dang, Y. Liu, Y. Sun, D. Yuan, X. Liu, W. Lu, G. Liu, H. Xia, X. Tao, *CrystEngComm* **2015**, *17*, 665.

[7] Z. Xu, Z. Liu, N. Li, G. Tang, G. Zheng, C. Zhu, Y. Chen, L. Wang, Y. Huang, L. Li, N. Zhou, J. Hong, Q. Chen, H. Zhou, *Adv. Mater.* **2019**, *31*, 1900390.

[8] L. Mao, W. Ke, L. Pedesseau, Y. Wu, C. Katan, J. Even, M. R. Wasielewski, C. C. Stoumpos, M. G. Kanatzidis, *J. Am. Chem. Soc.* **2018**, *140*, 3775.

[9] C. C. Stoumpos, D. H. Cao, D. J. Clark, J. Young, J. M. Rondinelli, J. I. Jang, J. T. Hupp, M. G. Kanatzidis, *Chem. Mater.* **2016**, *28*, 2852.

[10] J. Li, Z. Chen, S. Saha, J. K. Utterback, M. L. Aubrey, R. Yuan, H. L. Weaver, N. S. Ginsberg, K. W. Chapman, M. R. Filip, *J. Am. Chem. Soc.* **2022**, *144*, 22403.

[11] M. L. Aubrey, A. Saldivar Valdes, M. R. Filip, B. A. Connor, K. P. Lindquist, J. B. Neaton, H. I. Karunadasa, *Nature* **2021**, *597*, 355.

[12] a) S.-K. Yu, Z.-R. Zhang, Z.-H. Ren, H.-L. Zhai, Q.-Y. Zhu, J. Dai, *Inorg. Chem.* **2021**, *60*, 9132; b) P. Kour, M. Chenna Reddy, S. Pal, S. Sidhik, T. Das, P. Pandey, S. P. Mukherjee, S. Chakraborty, A. D. Mohite, S. Ogale, *Angew. Chem., Int. Ed.* **2021**, *60*, 18750.

[13] C. Atallah, C. Charcosset, H. Greige-Gerges, *Journal of Pharmaceutical Analysis* **2020**, *10*, 499.

[14] R. M. Silverstein, F. X. Webster, D. J. Kiemle, D. L. Bryce, *Spectrometric Identification of Organic Compounds /Robert M. Silverstein, Francis X. Webster, David J. Kiemle, State University of New York, College of Environmental Science and Forestry, David L. Bryce, University of Ottawa*, John Wiley and Sons, Inc, Hoboken, NJ **2015**.

[15] Z. Xia, L. Baird, N. Zimmerman, M. Yeager, *Appl. Surf. Sci.* **2017**, *416*, 565.

[16] J. Jimenez, M. A. Washington, J. L. Resnick, K. K. Nischal, M. V. Fedorchak, *Drug Delivery and Translational Research* **2021**, 1.

[17] J. Ferreira de Santana, A. Mirzahosseini, B. Noszál, *Journal of Spectroscopy* **2022**, *2022*, 1.

[18] M. Hasan, D. Bethell, M. Brust, *J. Am. Chem. Soc.* **2002**, *124*, 1132.

[19] M. Bhogadia, M. Edgar, K. Hunwin, G. Page, M. Grootveld, *Metabolites* **2023**, *13*, 792.

[20] D. Spirito, Y. Asensio, L. E. Hueso, B. Martín-García, *J. Phys.: Mater.* **2022**, *5*, 034004.

[21] D. Cortecchia, S. Neutzner, A. R. Srimath Kandada, E. Mosconi, D. Meggiolaro, F. De Angelis, C. Soci, A. Petrozza, *J. Am. Chem. Soc.* **2017**, *139*, 39.

[22] C. Quarti, G. Grancini, E. Mosconi, P. Bruno, J. M. Ball, M. M. Lee, H. J. Snaith, A. Petrozza, F. De Angelis, *J. Phys. Chem. Lett.* **2013**, *5*, 279.

[23] D. G. Castner, K. Hinds, D. W. Grainger, *Langmuir* **1996**, *12*, 5083.

[24] M. Šetka, R. Calavia, L. Vojkůvka, E. Llobet, J. Drbohlavová, S. Vallejos, *Sci. Rep.* **2019**, *9*, 8465.

[25] N. Mathews, C. Ángeles-Chávez, M. Cortés-Jácome, J. T. Antonio, *Electrochim. Acta* **2013**, *99*, 76.

[26] J. Chastain, R. C. King Jr., *Perkin-Elmer Corporation* **1992**, *40*, 221.

[27] S. Kerber, J. Bruckner, K. Wozniak, S. Seal, S. Hardcastle, T. Barr, *J. Vac. Sci. Technol., A* **1996**, *14*, 1314.

[28] C. Mohsen, Y. Ramin, J. Farid, S. Abdolhossein, M. Cheraghizade, R. Yousefi, F. Jamali-Sheini, *Majlesi Journal of Telecommunication Devices* **2013**, *2*, 21.

[29] A. A. Jarzęcki, *The Journal of Physical Chemistry A* **2012**, *116*, 571.

[30] A. D. Baranyi, R. Makhija, M. Onyszchuk, *Can. J. Chem.* **1976**, *54*, 1189.

[31] R. Warren, W. Liang, *J. Phys.: Condens. Matter* **1993**, *5*, 6407.

[32] K. Awsiuk, A. Psarouli, P. Petrou, A. Budkowski, S. Kakabakos, A. Bernasik, J. Rysz, I. Raptis, *Proc. Eng.* **2011**, *25*, 334.

[33] I. Spanopoulos, I. Hadar, W. Ke, P. Guo, E. M. Mozur, E. Morgan, S. Wang, D. Zheng, S. Padgaonkar, G. M Reddy, *J. Am. Chem. Soc.* **2021**, *143*, 7069.

[34] M. J. Trimpl, A. D. Wright, K. Schutt, L. R. Buizza, Z. Wang, M. B. Johnston, H. J. Snaith, P. Müller-Buschbaum, L. M. Herz, *Adv. Funct. Mater.* **2020**, *30*, 2004312.

[35] L. Mao, Y. Wu, C. C. Stoumpos, B. Traore, C. Katan, J. Even, M. R. Wasielewski, M. G. Kanatzidis, *J. Am. Chem. Soc.* **2017**, *139*, 11956.

[36] M. D. Smith, B. L. Watson, R. H. Dauskardt, H. I. Karunadasa, *Chem. Mater.* **2017**, *29*, 7083.

[37] Rigaku Corporation, **2024**.

[38] G. M. Sheldrick, *Acta Crystallographica Section A: Foundations and Advances* **2015**, *71*, 3.

[39] G. M. Sheldrick, *Acta Crystallographica Section C: Structural Chemistry* **2015**, *71*, 3.

[40] O. V. Dolomanov, L. J. Bourhis, R. J. Gildea, J. A. Howard, H. Puschmann, *J. Appl. Crystallogr.* **2009**, *42*, 339.

[41] K. Momma, F. Izumi, *J. Appl. Crystallogr.* **2011**, *44*, 1272.

[42] C. F. Macrae, I. Sovago, S. J. Cottrell, P. T. Galek, P. McCabe, E. Pidcock, M. Platings, G. P. Shields, J. S. Stevens, M. Towler, *Applied Crystallography* **2020**, *53*, 226.

[43] P. Giannozzi, O. Andreussi, T. Brumme, O. Bunau, M. B. Nardelli, M. Calandra, R. Car, C. Cavazzoni, D. Ceresoli, M. Cococcioni, *J. Phys.: Condens. Matter* **2017**, *29*, 465901.

[44] J. P. Perdew, K. Burke, M. Ernzerhof, *Phys. Rev. Lett.* **1996**, *77*, 3865.

[45] H. J. Monkhorst, J. D. Pack, *Phys. Rev. B* **1976**, *13*, 5188.

[46] A. Corso, *Comput. Mater. Sci.* **2014**, *95*, 337.